

SMERF: Streamable Memory Efficient Radiance Fields for Real-Time Large-Scene Exploration

Daniel Duckworth^{1*} Peter Hedman^{2*} Christian Reiser^{2,4,5} Peter Zhizhin²
Jean-François Thibert³ Mario Lučić¹ Richard Szeliski² Jon Barron²

¹ Google DeepMind ² Google Research ³ Google Inc.
⁴ Tübingen AI Center ⁵ University of Tübingen

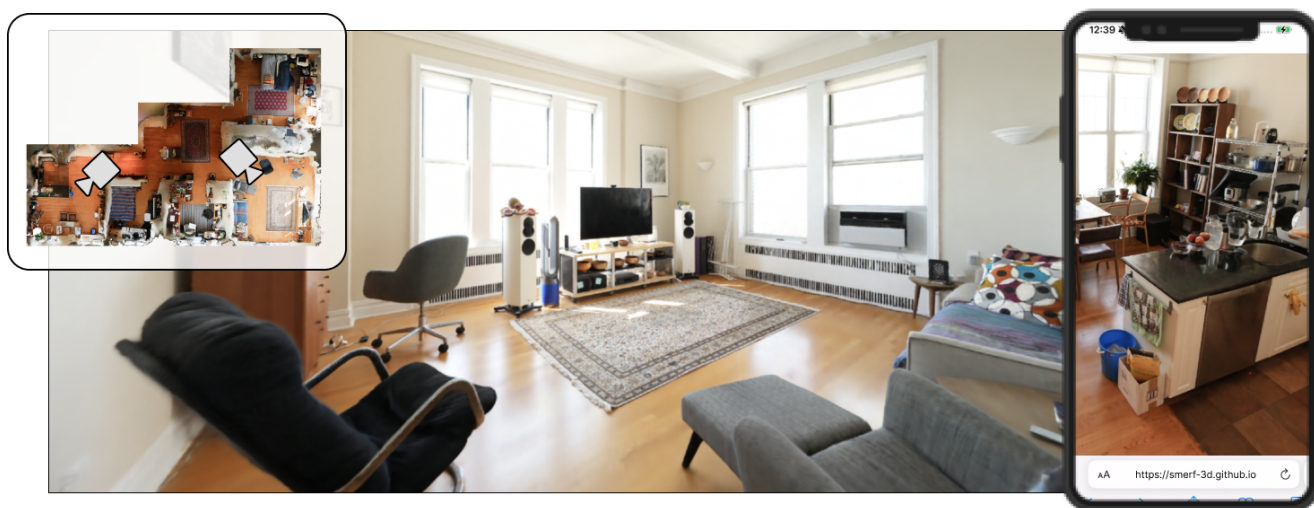


Figure 1. SMERF achieves real-time view-synthesis of large scenes across a wide variety of commodity devices while approaching the quality of state-of-the-art offline methods. By streaming in content based on viewpoint, our method scales to scenes of hundreds of m^2 and runs in the browser on resource-constrained devices, including smartphones.

Abstract

Recent techniques for real-time view synthesis have rapidly advanced in fidelity and speed, and modern methods are capable of rendering near-photorealistic scenes at interactive frame rates. At the same time, a tension has arisen between explicit scene representations amenable to rasterization and neural fields built on ray marching, with state-of-the-art instances of the latter surpassing the former in quality while being prohibitively expensive for real-time applications. In this work, we introduce SMERF, a view synthesis approach that achieves state-of-the-art accuracy among real-time methods on large scenes with footprints up to $300 m^2$ at a volumetric resolution of $3.5 mm^3$. Our method is built upon two primary contributions: a hierarchical model partitioning scheme, which increases model capacity while

constraining compute and memory consumption, and a distillation training strategy that simultaneously yields high fidelity and internal consistency. Our approach enables full six degrees of freedom (6DOF) navigation within a web browser and renders in real-time on commodity smartphones and laptops. Extensive experiments show that our method exceeds the current state-of-the-art in real-time novel view synthesis by 0.78 dB on standard benchmarks and 1.78 dB on large scenes, renders frames three orders of magnitude faster than state-of-the-art radiance field models, and achieves real-time performance across a wide variety of commodity devices, including smartphones. We encourage the reader to explore these models in person at our project website: <https://smerf-3d.github.io>.

*Denotes equal contribution.

1. Introduction

Radiance fields have emerged as a powerful, easily-optimized representation for reconstructing and re-rendering photorealistic real-world 3D scenes. In contrast to explicit representations such as meshes and point clouds, radiance fields are often stored as neural networks and rendered using volumetric ray-marching. This is simultaneously the representation’s greatest strength and its biggest weakness: neural networks can concisely represent complex geometry and view-dependent effects given a sufficiently large computational budget. As a volumetric representation, the number of operations required to render an image scales in the number of pixels rather than the number of primitives (e.g. triangles), with the best-performing models [6] requiring tens of millions of network evaluations. As a result, real-time approaches to radiance fields make concessions in quality, speed, or representation size, and it remains an open question if such a representation can be competitive with alternative approaches such as Gaussian Splatting [25].

Our work answers this question in the affirmative. We present a scalable approach to real-time rendering of large spaces at higher fidelity than previously possible. Not only does our method approach the quality of slower, state-of-the-art (SOTA) models in standard benchmarks, it is the first to convincingly render unbounded, multi-room spaces in real-time on commodity hardware. Crucially, our method achieves this with a memory budget independent of scene size and without compromising either image quality or rendering speed.

We use variant of Memory-Efficient Radiance Fields (MERF) [48], a compact representation for real-time view synthesis, as a core building block. We construct a hierarchical model architecture composed of self-contained MERF submodels, each specialized for a region of viewpoints in the scene. This greatly increases model capacity with bounded resource consumption, as only a single sub-model is necessary to render any given camera. Specifically, our architecture tiles the scene with submodels to increase spatial resolution and also tiles parameters within each sub-model region to more accurately model view-dependent effects. We find the increase in model capacity to be a double-edged sword, as our architecture lacks the inductive biases of state-of-the-art models that encourage plausible reconstructions. We therefore introduce an effective new distillation training procedure that provides abundant supervision of both color and geometry, including generalization to novel viewpoints and stable results under camera motion. The union of these two innovations enables the real-time rendering of large scenes with similar scale and quality to existing state-of-the-art work.

Concretely, our two main contributions are:

- A tiled model architecture for real-time radiance fields ca-

pable of representing large scenes at high fidelity on hardware ranging from smartphones to desktop workstations.

- A radiance field distillation training procedure that produces highly-consistent submodels with the generalization capabilities and inductive biases of an accurate but compute-heavy teacher.

2. Related Work

Neural Radiance Fields have seen explosive progress in recent years, and a complete review of related work is therefore challenging. Here, we only review papers directly related to our work, either as building blocks, or as sensible alternatives. For a more comprehensive overview, please see Tewari et al. [59].

Improving NeRF’s Speed. Although NeRF produced compelling results, it was severely lacking in terms of speed: training a model took multiple hours and rendering an image took up to 30 seconds [36]. Since then, much effort has been placed on accelerating NeRF’s training and inference.

Many works achieve real-time rendering by precomputing (*i.e.*, *baking*) NeRF’s view-dependent colors and opacities into sparse volumetric data structures [16, 21, 73, 76]. Other works show that rendering and/or training can be significantly accelerated by parameterizing a radiance field with a large dense [56, 68, 77], hashed [37] or low-rank voxel grid parameterization [9, 10], a grid of small MLPs [47], or a “polygon soup” of neural textures [11]. Alternatively, rendering can be accelerated by reducing the sample budget while carefully allocating volumetric samples to preserve quality [19, 27, 38, 66]

In general, there is a tension between render time and memory consumption. This was explored in MERF [48], which uses a combination of sparse and low-rank voxel grid representations to enable real-time rendering of unbounded scenes with a limited memory budget [48]. We build upon MERF and extend it to significantly larger environments while still retaining real-time performance and adhering to the tight memory constraints of commodity devices.

Improving NeRF’s Quality. In parallel, the community has improved NeRF reconstruction quality in many different ways, such as alleviating aliasing [4, 23], increasing model capacity without impacting compute [37], modeling unbounded scenes [5], and eliminating floaters [44]. Other works improve robustness to other challenges, such as inaccurate camera poses [29, 41, 54], limited supervision [39, 50, 69, 74], or outliers such as illumination changes, transient objects [32, 49], and scene motion [24, 40].

Most relevant for our work is Zip-NeRF [6], which uses multisampling to enable anti-aliasing for fast grid-based representations [37] and produces highly accurate reconstructions of large environments while remaining tractable to train and render. Although Zip-NeRF currently achieves

state-of-the-art quality on established benchmarks, a single high-resolution frame requires multiple seconds to render and the method is not suitable for real-time rendering applications. We therefore adopt the approach of distilling a high-fidelity Zip-NeRF model into a set of MERF-based submodels, thereby achieving quality comparable to Zip-NeRF at real-time rendering speeds. We also incorporate several quality improvements listed above, such as latent codes for changing illumination [32] and gradient scaling for alleviating floaters [44], with no impact to rendering speed; see the appendices.

Rasterization-based View-Synthesis. While NeRF methods synthesise views using per-pixel ray-marching, an alternative paradigm is per-primitive rasterization that leverages specialized GPU hardware. Early such view synthesis methods approximated geometry with triangle meshes and used image blending to model view-dependent appearance [7, 12, 13]. Later methods improved quality with neural appearance models [20, 30, 31] or neural mesh reconstruction [45, 51, 65, 75]. Recent methods model more detailed geometry by rasterizing overlapping meshes and either decoding [63] or compositing [11] the resulting buffers. Furthermore, for limited viewing volumes semi-transparency can be modeled with layered representations such as multi-plane images [15, 35, 42, 80].

GPU hardware also accelerates the rendering of point-based representations. Early methods synthesized views by decoding sparse point clouds with a U-Net [1, 52, 67], but struggled with frame-to-frame consistency during camera movement. This can be addressed by extending each point into a disc [43, 57] equipped with a soft reconstruction kernel [81]. Recent work showed that these soft point-based representations are amenable to gradient-based optimization and can model semi-transparency as well as view-dependent appearance [26, 79].

Most relevant to our work is 3D Gaussian Splatting [25] (3DGS) which improves visual fidelity, simplifies initialization, improves the run-time of soft point-based representations and is the current state-of-the-art for real-time view-synthesis. While 3DGS produces high-quality reconstructions in many scenes, optimization remains challenging, and carefully chosen heuristics are required for point allocation. This is evident in large scenes, where many regions lack sufficient point density. To achieve real-time training and rendering, 3DGS further relies on platform-specific features and low-level APIs. While recent re-implementations render 3DGS models on commodity hardware [28, 82], they rely on approximations to sort order and view-dependency whose impact on quality has not yet been evaluated. In concurrent work, LightGaussian [14] suffers a small reduction in visual fidelity to significantly decrease model size. In our experiments, we directly compare our cross-platform web viewer with the latest version of the official 3DGS viewer.

Large Scale NeRFs. Although NeRF models excel at reproducing objects and localized regions of a scene, they struggle to scale efficiently to larger scenes. For object-centric captures this can be ameliorated by reparameterizing the unbounded background regions of the scene to a bounded domain [5, 78]. Larger, multi-room scenes can be modeled by applying anti-aliasing techniques to hash grid-backed radiance fields [6, 72]. Another approach is to split the scenes into multiple regions and train a separate NeRF for each region [46, 60, 71]. This idea also facilitates real-time rendering of both objects [47] and room-scale scenes [70]. Scaling to extremely large scenes such as city blocks or entire urban environments, however, requires partitioning based on camera location into redundant, overlapping scene volumes [34, 58]. We extend the idea of camera-based partitioning to real-time view-synthesis: whereas existing models require expensive rendering and image blending from multiple submodels, we need only one submodel to render a given camera and leverage regularization during training to encourage mutual consistency.

Distillation and NeRF. A powerful concept in deep learning is that of *distillation* — training a smaller or more efficient *student* model to approximate the output of a more expensive or cumbersome *teacher* [17, 22]. This idea has been successfully applied to NeRFs in a variety of contexts such as (1) distilling a large MLP into a grid of tiny MLPs [47], (2) distilling an expensive NeRF MLP into a small “proposal” MLP that bounds density [5], or (3) distilling expensive secondary ray bounces into a lightweight model for inverse rendering [55]. Distillation has also been used to obviate expensive ray marching and facilitate real-time rendering by converting an entire NeRF scene into a light field model [2, 8, 18, 64] or a surface representation [45].

In this work, we distill the appearance and geometry of a large, high-quality Zip-NeRF model into a family of MERF-like submodels. Concurrent with our work, Hybrid-NeRF [61] also employs distillation for real-time view synthesis, albeit for a signed distance field.

3. Preliminaries

We begin with a brief review of MERF, which uses a mapping from 3D positions $\mathbf{x} \in \mathbb{R}^3$ to feature vectors $\mathbf{t} \in \mathbb{R}^8$. MERF parameterizes this mapping using a combination of high-resolution triplanes ($\mathbf{P}_x, \mathbf{P}_y, \mathbf{P}_z \in \mathbb{R}^{R \times R \times 8}$) and a low-resolution sparse voxel grid $\mathbf{V} \in \mathbb{R}^{L \times L \times L \times 8}$. A query point \mathbf{x} is projected on each of three axis-aligned planes and the underlying 2D grid is queried via bilinear interpolation. Additionally, a trilinear sample is taken from the sparse voxel grid. The resulting four 8-dimensional vectors are then summed together:

$$\mathbf{t}_{\text{MERF}}(\mathbf{x}) = \mathbf{P}_x(\mathbf{x}) + \mathbf{P}_y(\mathbf{x}) + \mathbf{P}_z(\mathbf{x}) + \mathbf{V}(\mathbf{x}). \quad (1)$$

This vector is then unpacked into three parts, which are independently rectified to yield a scalar density, a diffuse RGB color, and a feature vector that encodes view-dependence effects:

$$\tau = \exp(\mathbf{t}_1), \quad \mathbf{c} = \text{sigmoid}(\mathbf{t}_{2:4}), \quad \mathbf{f} = \text{sigmoid}(\mathbf{t}_{5:8}). \quad (2)$$

To render a pixel, a ray is cast from that pixel’s center of projection \mathbf{o} along the viewing direction \mathbf{d} , and sampled at a set of distances $\{t_i\}$ to generate a set of points along that ray $\mathbf{x}_i = \mathbf{o} + t_i \mathbf{d}$. As in NeRF [36], the densities $\{\tau_i\}$ are converted into alpha compositing weights $\{w_i\}$ implied by the numerical quadrature approximation for volume rendering [33, 36]:

$$w_i = T_i(1 - \exp(-\tau_i \delta_i)) \text{ where } T_i = \exp\left(-\sum_{j < i} \tau_j \delta_j\right), \quad (3)$$

where $\delta_i = t_{i+1} - t_i$ is the distance between adjacent samples. After alpha composition, the deferred shading approach from SNeRG [21] is used to decode the blended diffuse RGB colors $\sum_i w_i \mathbf{c}_i$ and the blended view-dependent color features $\sum_i w_i \mathbf{f}_i$ into the final pixel color with the help of the small MLP $h(\cdot; \theta)$:

$$\left(\sum_i w_i \mathbf{c}_i\right) + h\left(\sum_i w_i \mathbf{c}_i, \sum_i w_i \mathbf{f}_i, \mathbf{d}; \theta\right), \quad (4)$$

where θ are the MLP’s parameters.

In unbounded scenes, far-away content can be modelled coarsely. To achieve a resolution that drops off with the distance from the scene’s focus point, MERF applies a contraction function to each spatial position \mathbf{x} before querying the feature field:

$$\text{contract}(\mathbf{x})_d = \begin{cases} x_d & \text{if } \|\mathbf{x}\|_\infty \leq 1 \\ \frac{x_d}{\|\mathbf{x}\|_\infty} & \text{if } x_d \neq \|\mathbf{x}\|_\infty > 1 \\ \left(2 - \frac{1}{|x_d|}\right) \frac{x_d}{|x_d|} & \text{if } x_d = \|\mathbf{x}\|_\infty > 1 \end{cases} \quad (5)$$

4. Model

Although real-time view-synthesis methods like MERF perform well for a localized environment, they often fail to scale to large multi-room scenes. To this end, we present a hierarchical architecture. First, we partition the coordinate space of the entire scene into a series of blocks, where each block is modeled by its own MERF-like representation. Second, we introduce an additional nested partitioning of each block, wherein we partition the view-dependent deferred appearance MLP weights of each MERF-like primitive into its own set of partitions. Finally, we use feature gating (explained below) to modify the feature aggregation of

the underlying triplane- and sparse-grid primitives to more effectively reallocate the limited capacity of our submodels onto detailed parts of the scene. Our overall architecture can therefore be thought of as a three-level hierarchy: based on the camera origin, (1) we choose a block’s submodel, then within that submodel (2) we interpolate to produce deferred MLP parameters, and then when featurizing the input to that MLP, (3) we use feature-gating to selectively enable the high-resolution triplanes.

This greatly increases the capacity of our model without diminishing rendering speed or increasing memory consumption: even as total storage requirements increase with the number of submodels, only a single submodel is required to render a give frame. As such, when implemented on a graphics accelerator, our system maintains modest resource requirements comparable to MERF.

Coordinate Space Partitioning: While MERF offers sufficient capacity for faithfully representing medium-scale scenes, we found the use of a single set of triplanes limits its capacity and reduces image quality. In large scenes, numerous surface points project to the same 2D plane location, and the representation therefore struggles to simultaneously represent high-frequency details of multiple surfaces. Although this can be ameliorated by simply increasing the coarse 3D grid and fine 2D triplane resolutions, doing so significantly increases memory consumption and is prohibitively expensive in practice.

To increase model capacity without increasing memory consumption, we coarsely subdivide the scene into a 3D grid and associate each grid cell with an independent submodel in a strategy similar to Block-NeRF [58]. Each submodel is assigned its own contraction function (Equation 5) and is tasked with representing the region of the scene within its grid cell at high detail, while the region outside each submodel’s cell is modeled coarsely. Note that the entire scene is still represented by each submodel — the submodels differ only in terms of which region of the scene lies inside or outside of each submodel’s contraction region. As such, rendering an image only requires querying a *single submodel*, which means that only one submodel must be in memory at a time.

Formally, we shift and scale all training cameras to lie within a $[-K/2, K/2]^3$ cube, and then partition this cube into K^3 identical and tightly packed subvolumes of size $[-1, 1]^3$. We assign training cameras to submodels $\{\mathcal{S}_k\}$ by identifying the associated subvolume \mathbf{R}_k that each camera origin \mathbf{o} lies within,

$$s^* = \arg \min_{k \in \{1..K^3\}} D(\mathbf{o}, k) \quad (6)$$

$$D(\mathbf{o}, k) = \min_{\mathbf{x} \in \mathbf{R}_k} \|\mathbf{o} - \mathbf{x}\|_\infty \quad (7)$$

We design our camera-to-submodel assignment procedure to apply to cameras outside of the training set, such as dur-

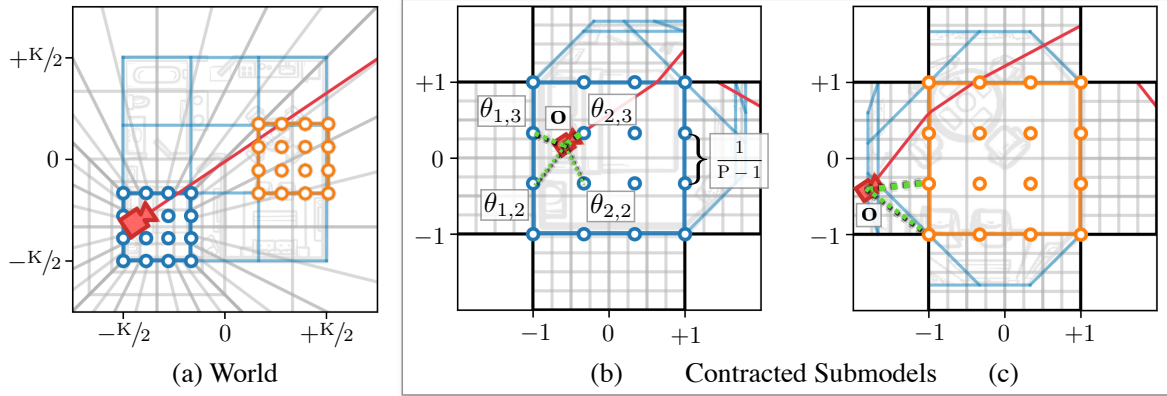


Figure 2. **Coordinate systems** in SMERF for a scene with $K = 3$ coordinate space partitions and $P = 4$ deferred appearance network subpartitions. Each partition is capable of representing the entire scene while allocating the majority of its model capacity to its corresponding partition. Within each partition, we instantiate a set of spatially-anchored MLP weights $\{\theta_{i,j}\}$ parameterizing the deferred appearance model, which we **trilinearly interpolate** as a function of the **camera** origin \mathbf{o} during rendering. In (a), we present the entire scene in world coordinates with the **scene partition** and highlight **two submodels**. In (b) and (c) we present the same scene from the view of two submodels in their corresponding contracted coordinate systems. (b) visualizes the rendering and parameter interpolation process when the camera origin \mathbf{o} lies **inside** of a submodel’s partition, and (c) visualizes the same when it lies **outside**.

ing test set rendering. This enables a wide range of features including ray jittering, submodel reassignment, the consensus loss, arbitrary test camera placement, and ping-pong buffering as described in Sections 5 and 6.

Rather than naively instantiating submodels for all K^3 subvolumes, we limit ourselves to subvolumes containing at least one camera from the training set. As most scenes are outdoor or single-story buildings, this reduces the number of instantiated submodels from K^3 to $O(K^2)$.

Deferred Appearance Network Partitioning: The second level in our partitioning hierarchy concerns the deferred rendering model. Recall that MERF employs a small multi-layer perceptron (MLP) to decode view-dependent colors from blended features as described in Equation (4). Although the small size of this network is critical for fast inference, we observed that its capacity is often insufficient to accurately reproduce complex view-dependent effects common to larger scenes. Simply increasing the size of the network is not viable as doing so would significantly reduce rendering speed.

Instead, we uniformly subdivide the domain of each submodel into a grid with P vertices along each axis. For each cell $(u, v, w) \in \{1, \dots, P\}^3$, we associate a separate set of network parameters θ_{uvw} . We assign parameters to cameras via trilinear interpolation based on camera origin \mathbf{o} ,

$$\theta = \text{Trilerp}(\mathbf{o}, \{\theta_{uvw} : (u, v, w) \in \{1, \dots, P\}^3\}) \quad (8)$$

The use of trilinear interpolation, unlike the nearest-neighbor interpolation used in our spatial partitioning, is critical in preventing aliasing of the view-dependent MLP parameters, which takes the form of conspicuous “popping”

artifacts in specular highlights as the camera moves through space. After parameter interpolation, view-dependent colors are decoded according to Equation (4).

Since the size of the view-dependent MLP is negligible compared to total representation size, deferred network partitioning has almost no effect on memory consumption or storage impact. As a result, this technique increases model capacity almost for free. This is contrast to coordinate space partitioning, which significantly increases storage size. We find that the union of coordinate space and deferred network partitioning is critical for effectively increasing spatial and view-dependent resolution, respectively. See Figure 2 for a visualization of these two forms of partitioning.

Feature Gating: The final level in our hierarchy is at the level of MERF’s coarse 3D voxel grid \mathbf{V} and three high-resolution triplanes ($\mathbf{P}_x, \mathbf{P}_y, \mathbf{P}_z$). In MERF, each 3D position is associated with an 8-dimensional feature vector, which is the sum of three vectors interpolated from the three triplanes and one vector interpolated from the coarse 3D grid (Equation (1)). Though largely effective, the features generated by this procedure are limited by their naive use of summation to merge high-resolution and low-resolution information, entangling the two together.

We instead elect to use low-resolution 3D features to “gate” high-resolution features: if high-resolution features add value for a given 3D coordinate, they should be employed, and otherwise, they should be ignored and the smoother, low-resolution features should be employed. To this end, we modify feature aggregation as follows: Before summing the 4 feature vectors, we split out the last component $\mathbf{V}(\mathbf{x})_8$ of the 8-dimensional feature vector queried

from the 3D voxel grid, and we multiply it into each triplane feature:

$$\hat{\mathbf{t}}(\mathbf{x}) = (\mathbf{P}_x(\mathbf{x}) + \mathbf{P}_y(\mathbf{x}) + \mathbf{P}_z(\mathbf{x})) \circ \mathbf{V}(\mathbf{x})_8 + \mathbf{V}(\mathbf{x}). \quad (9)$$

We then build our final feature by concatenating the aggregated feature $\hat{\mathbf{t}}(\mathbf{x})$ and the voxel grid feature $\mathbf{V}(\mathbf{x})$:

$$\mathbf{t}(\mathbf{x}) = \hat{\mathbf{t}}(\mathbf{x}) \oplus \mathbf{V}(\mathbf{x}). \quad (10)$$

Intuitively, this incentivizes the model to leverage the low-resolution voxel grid to disable the high-resolution triplanes when rendering low-frequency content, such as featureless white walls, and gives the model the freedom to focus on detailed parts of the scene. This change can also be thought of as a sort of ‘‘attention’’, as a multiplicative interaction is being used to determine when the model should ‘‘attend’’ to the triplane features [62]. This change slightly affects the memory and speed of our model by virtue of increasing the number of rows in the first weight matrix of our MLP, but the practical impact of this is negligible.

5. Training

5.1. Radiance Field Distillation

NeRF-like models such as MERF are traditionally trained ‘‘from scratch’’ to minimize photometric loss on a set of posed input images. A critical component when training such a system is regularizing the model to improve generalization to novel views. One example of this is Zip-NeRF [6], which employs a family of carefully tuned losses in addition to photometric reconstruction error to achieve state-of-the-art performance on large, multi-room scenes. We instead adopt ‘‘student/teacher’’ *distillation* [22] and train our representation to imitate an already-trained state-of-the-art radiance field model. In particular, we employ a higher-quality variant of Zip-NeRF [6]; see the appendices.

Distillation has several advantages: We inherit the helpful inductive biases of the teacher model, circumvent the need for manually tuning hyperparameters to maximize generalization, and enable the recovery of local representations that are globally-consistent. We show that our approach achieves quality comparable to its Zip-NeRF teacher while being three orders of magnitude faster to render.

We supervise our model by separately distilling the appearance and geometry of a reference radiance field. Note that the weights of the teacher model are frozen during optimization. See Figure 3 for a visualization.

Appearance: As in prior work, we supervise our model by minimizing the photometric difference between patches predicted by our model and a source of ground-truth image patches. Instead of limiting training to a set of photos representing a small subset of a scene’s plenoptic function, our source of ‘‘ground-truth’’ image patches is a teacher

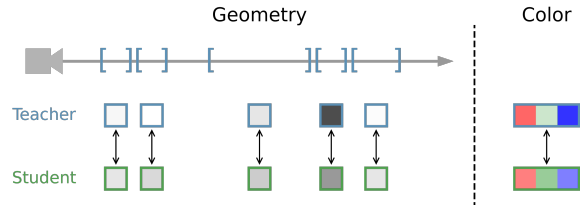


Figure 3. **Teacher Supervision.** The teacher model provides photometric supervision via rendered colors and geometric supervision via the volumetric weights along camera rays. Both teacher and student operate on the same set of ray intervals.

model rendered from an *arbitrary* set of cameras. We distill appearance by penalizing the discrepancy between 3×3 patches rendered from student and teacher models. In particular, we employ a weighted combination of the RMSE and DSSIM [3] metrics between each student patch \mathbf{C} and its corresponding teacher patch \mathbf{C}^* :

$$\mathcal{L}_c = 1.5 \cdot \text{DSSIM}(\mathbf{C}, \mathbf{C}^*) + \sum_{\mathbf{c} \in \mathbf{C}} \|\mathbf{c} - \mathbf{c}^*\|_2. \quad (11)$$

Geometry: To distill geometry, we begin by querying our teacher with a given ray origin and direction. This yields a set of weighted intervals along the camera ray $\{((t_i, t_{i+1}), w_i^T)\}$, where each (t_i, t_{i+1}) are the metric distances along the ray corresponding to interval i , and each w_i^T is the teacher’s corresponding alpha compositing weight for that interval as per Equation 3. The weight of each interval i reflects how much the corresponding interval contributed to the final predicted radiance. It is this quantity we distill into our student.

Mip-NeRF 360 [5] addressed the problem of distilling volumetric density from one model to another from a measure-theoretic perspective: the overlapping intervals along a ray are used to bound a student’s weights by a teacher’s, and any surplus weight that violates the bound imposed by the teacher is penalized. We adopt a similar approach, but in our setting we have the luxury of being able to select the set of intervals used by the student. In particular, we choose the same set of intervals $\{(t_i, t_{i+1})\}$ used by the teacher. This yields a set of student weights $\{w_i^S\}$ on which we impose a similar loss function to mip-NeRF 360’s: a penalty on the absolute value of the excess mass imposed by the upper and lower bounds of the teacher model. As our student and teacher models use the same set of intervals, this loss simplifies to the absolute difference between the teacher and student weights:

$$L_\tau = \sum_i |w_i^T - w_i^S|. \quad (12)$$

Because these volumetric rendering weights are a function of volumetric density (as per Equation 3), this loss on

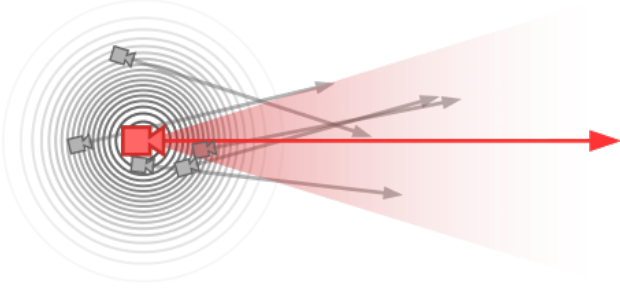


Figure 4. **Ray jittering.** To generate training rays for our student model (shown in gray) we randomly perturb the origins and directions of the camera rays of the input imagery used to supervise our teacher model (shown in red).

weights indirectly encourages the student’s and teacher’s density fields to be consistent with each other in visible regions of the scene.

5.2. Data Augmentation

Because our distillation approach allows us to supervise our student model at *any* ray in Euclidean space, we require a procedure for selecting useful random rays. While sampling rays uniformly at random throughout the scene is viable, this approach leads to poor reconstruction quality as many such rays originate from inside of objects or walls or are pointed towards unimportant or under-observed parts of the scene. Using camera rays corresponding to pixels in the dataset used to train the teacher model also performs poorly, as those input images represent a tiny subset of possible views of the scene. As such, we adopt a compromise approach of using randomly-perturbed versions of the input camera rays, which yields a kind of “data augmentation” that improves generalization while still focusing the student model’s attention towards the parts of the scene that the camera operator deemed relevant.

To generate a training ray we first randomly select a ray from the teacher’s dataset parameterized by an origin \mathbf{o} and direction \mathbf{d} . We then jitter the origin with isotropic Gaussian noise, and draw a uniform sample from an ϵ -neighborhood of the ray’s direction vector to obtain a ray $(\hat{\mathbf{o}}, \hat{\mathbf{d}})$:

$$\hat{\mathbf{o}} \sim \mathcal{N}(\mathbf{o}, \sigma^2 \mathbb{I}), \quad (13)$$

$$\hat{\mathbf{d}} \sim \mathcal{U}(\{\mathbf{v} \in \mathbb{R}^3 : \|\mathbf{v} - \mathbf{d}\|_2 < \epsilon, \|\mathbf{v}\|_2 = 1\}). \quad (14)$$

In all experiments, we set $\sigma = 0.03$ and $\epsilon = 0.03$ (note that σ is defined in normalized scene coordinates, where all the input cameras live inside the $[-1, 1]^3$ cube). See Figure 4 for a visualization of this procedure.

5.3. Submodel Consistency

Recall that, in spite of employing a single teacher model, coordinate space partitioning means that we are effectively training multiple, independent student submodels in parallel (though in practice, all submodels are trained simultaneously on a single machine). This presents a challenge in terms of *consistency* across submodels — at test time, we do not want the appearance of the scene to abruptly change when switching from one submodel to another. This problem has been ameliorated in the past by rendering from multiple submodels and blending their results [58], but that solution significantly slows down rendering and requires multiple submodels to be in-memory simultaneously. In contrast, for the sake of performance and memory constraints, we aim to render each frame while only storing and querying a *single* submodel.

To encourage adjacent submodels to make similar predictions for a given camera ray, we introduce a photometric consistency loss between submodels. During training we render each camera ray in our batch twice: once using its “home” submodel s (whichever submodel the ray origin lies within the interior of), and again using a randomly-chosen neighboring submodel \hat{s} . We then impose a straightforward loss between those two rendered colors, thereby encouraging them to resemble each other:

$$\mathcal{L}_s = \|\mathbf{c}_s(\mathbf{r}) - \mathbf{c}_{\hat{s}}(\mathbf{r})\|_2. \quad (15)$$

Additionally, when constructing batches of the training rays generated in Section 5.2, we take care to assign each ray to a submodel where it will meaningfully improve reconstruction quality. Intuitively, we expect rays to add the most value to their “home” submodel, but the rays that originate from neighboring submodels may also provide value by providing additional viewing angles of scene content with each submodel’s interior. As such, when constructing a batch of training data, we first assign each training ray its “home” submodel, and then randomly re-assign 20% of the batch to a randomly-selected adjacent submodel.

6. Rendering

Baking. After training we generate and store a set of precomputed assets that will be used for real-time rendering. We follow MERF [48] when baking these assets, but slightly augment the culling step that discards voxels that did not contribute to any of the training images: We post-process the resulting culling mask with a small 3^3 median filter that simultaneously closes small holes and also reduces storage by discarding small false-positive floaters.

We produce an independent set of baked assets for each submodel where each asset is similar to MERF: the feature maps for the three high-resolution 2D planes and the low-resolution sparse voxel grids are stored as quantized byte

arrays, and the remaining deferred network parameters are stored as floating point arrays. We store these assets as gzip-compressed binary blobs, which we found to be slightly smaller and significantly faster to decode than PNG images.

Live Viewer. After baking assets, we render our model using a carefully-designed real-time rendering engine designed to operate on a wide range of commodity hardware including smartphones, laptops, and desktops. We primarily achieve low resource usage by our design decision to train up to K^3 individual submodels such that every submodel contains a contracted representation of the full scene. As a result, only one submodel (whichever submodel encloses the center of projection of the view being rendered) is needed in memory at any point time, bounding the memory requirements of our model.

To hide network latency, submodels are “hot swapped” in and out of memory as the user interactively explores the environment. When the camera of the interactive viewer moves into a new subvolume, the corresponding submodel is loaded into host memory, while the previous submodel, which includes an approximate model of the geometry of this new adjacent region, continues to be used for rendering. Once the new submodel is available, we transfer it to video memory begin using it for rendering. Peak GPU memory is thus limited to a maximum of two submodels: one actively being rendered and one being loaded into memory. We further limit host memory usage by evicting loaded submodels from memory using a least-recently used caching scheme.

The active submodel is rendered similarly to MERF. Texture look-ups are used to retrieve feature representations and density, and an OpenGL fragment shader is used for ray marching and deferred rendering. We diverge from MERF in the use of a *distance grid* for accelerating ray marching in free space: whereas MERF uses several binary occupancy grids to determine if a voxel is occupied or not, we use a single distance grid that stores an 8-bit distance to the nearest occupied voxel. The renderer thus rapidly skips large distances along each ray without the need for expensive hierarchical ray/box intersection tests. As a result, our renderer achieves significantly higher frame rates while guaranteeing identical results. We also employ optimized shader code for improved performance (see the appendices).

While interpolating our deferred appearance network parameters requires extra compute, this ultimately has a negligible effect on frame render time. The interpolation procedure need only be performed once per frame and is common to all pixels in an image. In practice, we perform this interpolation on CPU before executing the fragment shader.

7. Experiments

We evaluate our model’s performance and quality primarily by comparing it against two state-of-the-art methods: 3D Gaussian Splatting [25] and Zip-NeRF [6]. Zip-NeRF pro-

Method Metric	PSNR↑	SSIM↑	LPIPS↓	FPS↑	Mem (MB)↓	Disk (MB)↓
MERF (ours)	23.49	0.746	0.444	283	522	128
3DGS	25.50	0.810	0.369	441	227	212
Ours (K = 1)	25.44	0.777	0.412	329	505	118
Ours (K = 3)	27.09	0.823	0.350	220	1313	1628
Ours (K = 5)	27.28	0.829	0.339	204	1454	4108
Zip-NeRF	27.37	0.836	0.305	0.25	-	607

Table 1. Quantitative results on the large scenes from Zip-NeRF [6]. As the spatial subdivision resolution K increases, our accuracy approaches that of the Zip-NeRF “teacher”.

Method Metric	PSNR↑	SSIM↑	LPIPS↓	FPS↑	Mem (MB)↓	Disk (MB)↓
BakedSDF	24.51	0.697	0.309	507	573	457
iNGP	25.68	0.706	0.302	8.61	-	104
3DGS	27.20	0.815	0.214	260	780	740
MERF (published)	25.24	0.722	0.311	162	400	162
MERF (ours)	24.95	0.728	0.302	278	504	153
Ours (K = 1)	27.98	0.818	0.212	217	466	139
Zip-NeRF	28.78	0.836	0.177	0.25	-	607

Table 2. Quantitative results on the mip-NeRF 360 dataset [5].

	PSNR↑	SSIM↑	LPIPS↓	Disk (MB)↓	
Distill.	No Color Supervision	26.25	0.768	0.268	140
	No Geometry Supervision	27.67	0.805	0.229	164
	No Ray Jittering	26.22	0.769	0.267	125
Optim.	No SSIM Loss	27.62	0.806	0.227	154
	25k Train Steps	27.55	0.803	0.231	158
	No Larger Hash Grids	27.71	0.808	0.226	156
	No Hyperparam. Tuning	26.96	0.779	0.254	161
Model	No MLP Grid	27.10	0.803	0.228	154
	No Total Var. Reg.	27.75	0.810	0.223	154
	No Feature Gating	27.38	0.801	0.229	145
	No Median filter	27.75	0.811	0.222	165
Ablation base: 50k steps					
Ours: 200k steps					

Table 3. Ablation study of our model without subdivision ($K = 1$) on the mip-NeRF 360 dataset [5]. Note that we use a weaker version of our method for these experiments; see the appendices.

duces the highest-quality renderings of any radiance field model but is too slow to be useful in real-time contexts, while 3DGS renders quickly but produces lower-quality renderings than Zip-NeRF. We show that our model is, (1) comparable to 3DGS in runtime when GPUs are available, (2) capable of running in real-time on a wide range of commodity hardware platforms, and (3) significantly more accurate than 3DGS. We do not aim to outperform Zip-NeRF in terms of quality – Zip-NeRF is our model’s teacher, and represents an *upper bound* on achievable image quality.

Reconstruction Quality. We first evaluate our method on four large scenes introduced by Zip-NeRF: BERLIN, ALAMEDA, LONDON, and NYC. Each of these scenes was captured with 1,000-2,000 photos using a 180° fish-eye lens. To produce an apples-to-apples comparison with 3DGS, we crop photos to a 110° field-of-view and reestimate camera parameters with COLMAP [53]. Images are then downsampled to a resolution between 1392×793 and

2000 × 1140, depending on scene. Because this is a recent dataset without many established benchmark numbers, we limit evaluations to our method, 3DGS, Zip-NeRF, and MERF. As some scenes in this dataset exhibits variable auto-exposure across images, we modify our algorithm and all baselines accordingly (see the appendices).

The results shown in Table 1 indicate that, for modest degrees of spatial subdivision K , the accuracy of our method strongly surpasses that of MERF and 3DGS. As K increases, our model’s reconstruction accuracy improves and approaches that of its Zip-NeRF teacher, with a gap of less than 0.1 PSNR and 0.01 SSIM at $K = 5$.

We find that these quantitative improvements understate the qualitative improvements in reconstruction accuracy, as demonstrated in Figure 5. In large scenes, our method consistently models thin geometry, high-frequency textures, specular highlights, and far-away content where the real-time baselines fall short. At the same time, we find that increasing submodel resolution naturally increases quality, particularly with respect to high-frequency textures: see Figure 7. In practice, we find our renders to be virtually indistinguishable from Zip-NeRF, as shown in Figure 8.

We further evaluate our method on the mip-NeRF 360 dataset of unbounded indoor and outdoor scenes [5]. These scenes are much smaller than those in the Zip-NeRF dataset, and as such, spatial subdivision is unnecessary to achieve high quality results. As shown in Table 2, the $K = 1$ version of our model outperforms all prior real-time models on this benchmark in terms of image quality with a rendering speed comparable to that of 3DGS. Note that we significantly improve upon the MERF baseline despite the lack of spatial subdivision, which demonstrates the value of the our deferred appearance network partitioning and feature gating contributions. Figures 6 and 8 illustrate this improvement qualitatively: our method is far better at representing high-frequency geometry and textures while eliminating distracting floaters and fog.

Rendering Speed. We report frame rate numbers at native dataset resolution in Tables 1 and 2. We benchmark a scene by rendering each image in the test set 100x on a GPU-

Device Resolution	Frames per Second		
	iPhone 380 × 640	Macbook 1280 × 720	Desktop 1920 × 1080
BakedSDF	-	108	412
MERF (published)	38.1	32	113
MERF (ours)	58.3	47.6	187
3DGS	-	-	176
Ours ($K = 1$)	55.4	42.5	142

Table 4. Rendering speeds for different devices and resolutions, averaged across outdoor mip-NeRF 360 scenes. Our method achieves real-time rendering rates on all hardware platforms, including smartphones. See the appendices for hardware specs. Not all methods are capable of running on all platforms.

equipped workstation (Desktop, the appendices) and computing the arithmetic mean of frame rendering times (*i.e.*, the harmonic mean of FPS).

In Table 4, we report the performance of several recent methods as a function of image resolution and hardware platform. Our model is able to run in real-time on smartphones and laptops, albeit at reduced resolutions. MERF and BakedSDF [75] are also capable of running on resource-constrained platforms, but their reconstruction quality significantly lags behind ours; see Tables 1 and 2. We omit results for BakedSDF on iPhone due to memory limitations and 3DGS on iPhone and MacBook due to the lack of an official implementation for non-CUDA devices. While 3DGS modestly outperforms our cross-platform web viewer in terms of rendering speed on a desktop workstation, Tables 1 and 2 indicate that its reconstruction quality lags behind our method.

Ablations. In Table 3, we present an ablation study showing the effect of independently disabling various contributions regarding distillation, optimization, and model architecture on the mip-NeRF 360 dataset. In Figure 6 and Table 5, we bundle these improvements by category and incrementally add them to MERF to produce our model. We find that each markedly increases visual fidelity, bridging the gap between MERF and ground-truth photos.

In Table 5, we demonstrate the quality and memory characteristics of our method and a series of MERF variants as a function of spatial resolution. While the in-memory representation size of baseline methods grows with spatial resolution and eventually runs out of memory, ours is bounded by the size of the two largest submodels. At the same time, our method achieves strictly higher quality at all resolutions, which generally continues to improve as the number of coordinate space partitions increases.

In Figure 9, we demonstrate the effectiveness of our approach to submodel consistency. Although the same view is rendered by four distinct submodels, we find their outputs to be virtually indistinguishable.

Limitations. While our method performs admirably in terms of reconstruction quality and memory usage, it comes with a high storage cost. In the live viewer, this surfaces in the form of loading events and high network usage. Our method also incurs a non-trivial training cost: in addition to the cost of teacher training, we optimize our method for 100-200,000 steps on 8x V100 or 16x A100 GPUs, depending on the dataset. In terms of reconstruction quality, our method performs better than 3DGS on average, but is not universally higher in detail on all parts of all scenes. We attribute this to the voxel structure imposed on the scene by our representation.

Summary. Overall, our model is capable of running across a wide range of hardware platforms at real-time rates while

	Spatial Res. K	2048 ³		4096 ³		6144 ³		8192 ³		10240 ³	
		PSNR↑	Mem↓	PSNR↑	Mem↓	PSNR↑	Mem↓	PSNR↑	Mem↓	PSNR↑	Mem↓
MERF (ours)	1	23.14	433	23.71	1974	23.77	5590	23.74	12119	-	-
MERF+D	1	24.14	460	24.96	2042	25.23	5745	25.28	12684	-	-
MERF+DO	1	24.43	478	25.29	2168	25.52	6061	25.59	13198	-	-
Ours	Varies	25.28	428	26.36	953	26.85	1067	26.84	1076	27.06	1156

Table 5. Spatial resolution. We compare our method to monolithic variants of MERF with distillation (MERF+D) and optimization (MERF+DO) contributions with increased triplane and sparse grid resolutions. Rather than increasing the same parameters, our method achieves higher spatial resolution via increased submodel subdivision resolution $K = \{1..5\}$. Our method achieves universally higher quality and greater spatial resolution while bounding memory usage by the size of the two largest submodels. Note that, in contrast to our headline results, this ablation is based on a slightly weaker model that is faster to train; see the appendices for details.

producing state-of-the-art quality renderings among all real-time radiance field methods. We encourage the reader to visit the demo on our project page to experience this real-time rendering first-hand: <https://smerf-3d.github.io>.

8. Conclusion

In this work, we presented SMERF, a streamable, memory-efficient radiance field representation for real-time view-synthesis of large scenes. Our method renders in real-time in the web browser on everyday, resource-constrained consumer devices including smartphones and laptops. At the same time, our method achieves state-of-the-art quality compared to existing real-time methods on both medium and large scenes, exceeding the existing state-of-the-art by 0.78 and 1.78 dB PSNR, respectively. In the large scene setting, our quality is nearly indistinguishable from Zip-NeRF, the current state-of-the-art in offline view-synthesis.

We achieve this by distilling a high-fidelity Zip-NeRF teacher into a hierarchical student built on MERF. Our method subdivides scenes into independent submodels, each of which is further subdivided into a set of deferred rendering networks. As a consequence, only a single submodel and a local neighborhood of deferred network parameters are required to render a target view. We further introduce a series of improvements to MERF’s viewer, increasing frame rates by over 70%. As a result, memory and compute requirements remain on-par with MERF while markedly increasing quality and rendering speed.

Acknowledgements. We would like to thank Dor Verbin, Pratul Srinivasan, Ben Mildenhall, Klaus Greff, Alexey Dosovitskiy, Marcos Seefelder, and in particular Stephan Garbin for discussions and valuable feedback throughout the project. We would also like to sincerely thank Georgios Kopanas and Bernhard Kerbl for their generous help with tuning 3DGS and verifying our results. We would further like to thank Oliver Unke for his knowledge of differential geometry as applied to data augmentation and Ilies Ghanzouri for his contributions to the live renderer. Finally, we would like to thank Jane Kasdano for her valuable feedback on the design and presentation of this work.

References

- [1] Kara-Ali Aliev, Artem Sevastopolsky, Maria Kolos, Dmitry Ulyanov, and Victor Lempitsky. Neural point-based graphics. *Computer Vision—ECCV 2020: 16th European Conference, Glasgow, UK, August 23–28, 2020, Proceedings, Part XXII 16*, 2020.
- [2] Benjamin Attal, Jia-Bin Huang, Michael Zollhöfer, Johannes Kopf, and Changil Kim. Learning neural light fields with ray-space embedding networks. *CVPR*, 2022.
- [3] Allison H. Baker, Alexander Pinard, and Dorit M. Hammerling. DSSIM: a structural similarity index for floating-point data, 2023.
- [4] Jonathan T. Barron, Ben Mildenhall, Matthew Tancik, Peter Hedman, Ricardo Martin-Brualla, and Pratul P. Srinivasan. Mip-NeRF: A multiscale representation for anti-aliasing neural radiance fields. *ICCV*, 2021.
- [5] Jonathan T. Barron, Ben Mildenhall, Dor Verbin, Pratul P. Srinivasan, and Peter Hedman. Mip-NeRF 360: Unbounded anti-aliased neural radiance fields. *CVPR*, 2022.
- [6] Jonathan T. Barron, Ben Mildenhall, Dor Verbin, Pratul P. Srinivasan, and Peter Hedman. Zip-NeRF: Anti-aliased grid-based neural radiance fields. *ICCV*, 2023.
- [7] Chris Buehler, Michael Bosse, Leonard McMillan, Steven Gortler, and Michael Cohen. Unstructured Lumigraph rendering. *SIGGRAPH*, 2001.
- [8] Junli Cao, Huan Wang, Pavlo Chemerys, Vladislav Shakhrai, Ju Hu, Yun Fu, Denys Makoviichuk, Sergey Tulyakov, and Jian Ren. Real-time neural light field on mobile devices. *CVPR*, 2023.
- [9] Eric R. Chan, Connor Z. Lin, Matthew A. Chan, Koki Nagano, Boxiao Pan, Shalini De Mello, Orazio Gallo, Leonidas Guibas, Jonathan Tremblay, Sameh Khamis, Tero Karras, and Gordon Wetzstein. Efficient geometry-aware 3D generative adversarial networks. *CVPR*, 2022.
- [10] Anpei Chen, Zexiang Xu, Andreas Geiger, Jingyi Yu, and Hao Su. TensorRF: Tensorial radiance fields. *ECCV*, 2022.
- [11] Zhiqin Chen, Thomas Funkhouser, Peter Hedman, and Andrea Tagliasacchi. MobileNeRF: Exploiting the polygon rasterization pipeline for efficient neural field rendering on mobile architectures. *CVPR*, 2023.
- [12] Abe Davis, Marc Levoy, and Fredo Durand. Unstructured light fields. *Comput. Graph. Forum*, 2012.
- [13] Paul Debevec, Yizhou Yu, and George Borshukov. Efficient view-dependent image-based rendering with projective texture-mapping. *EGSR*, 1998.

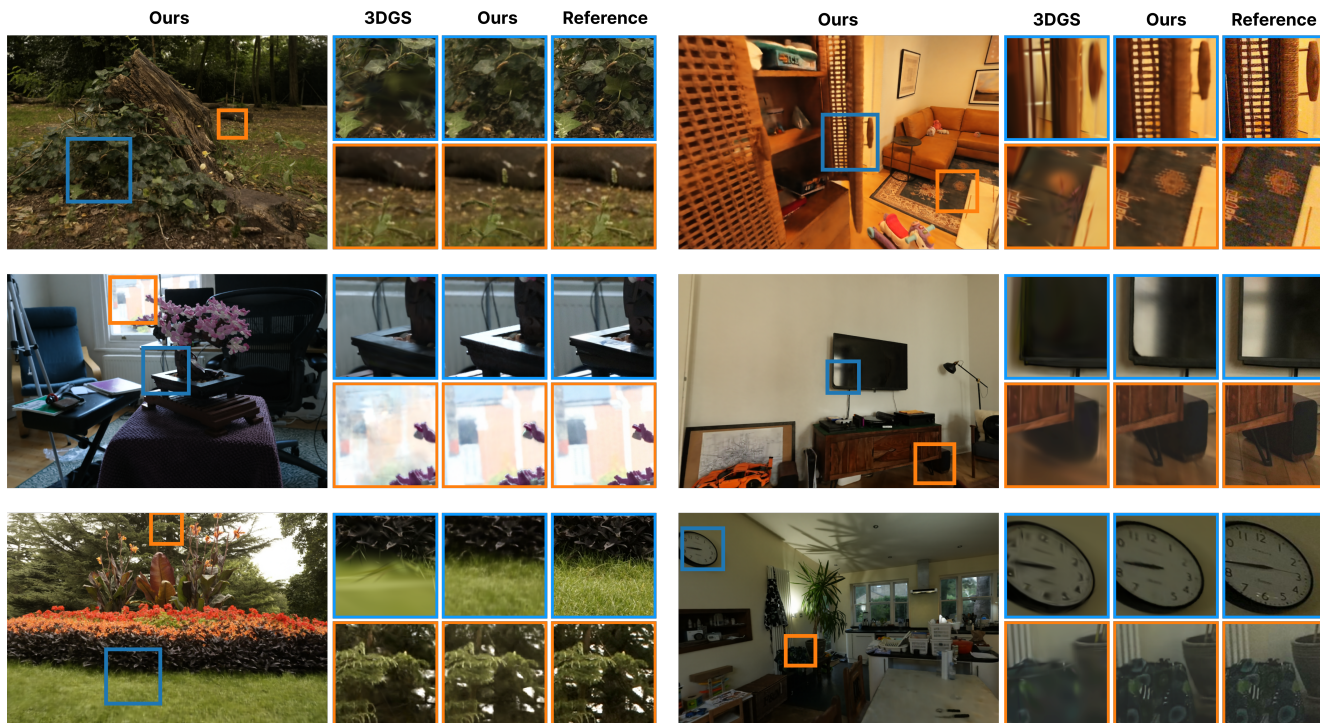


Figure 5. **Qualitative comparison.** We show results from our model and from 3D Gaussian Splatting [25] alongside ground-truth images on scenes from the mip-NeRF 360 [5] (left) and Zip-NeRF [6] (right) datasets. 3D Gaussian Splatting struggles to reproduce the thin geometry, high-frequency textures, and view-dependent effects which our model successfully recovers.

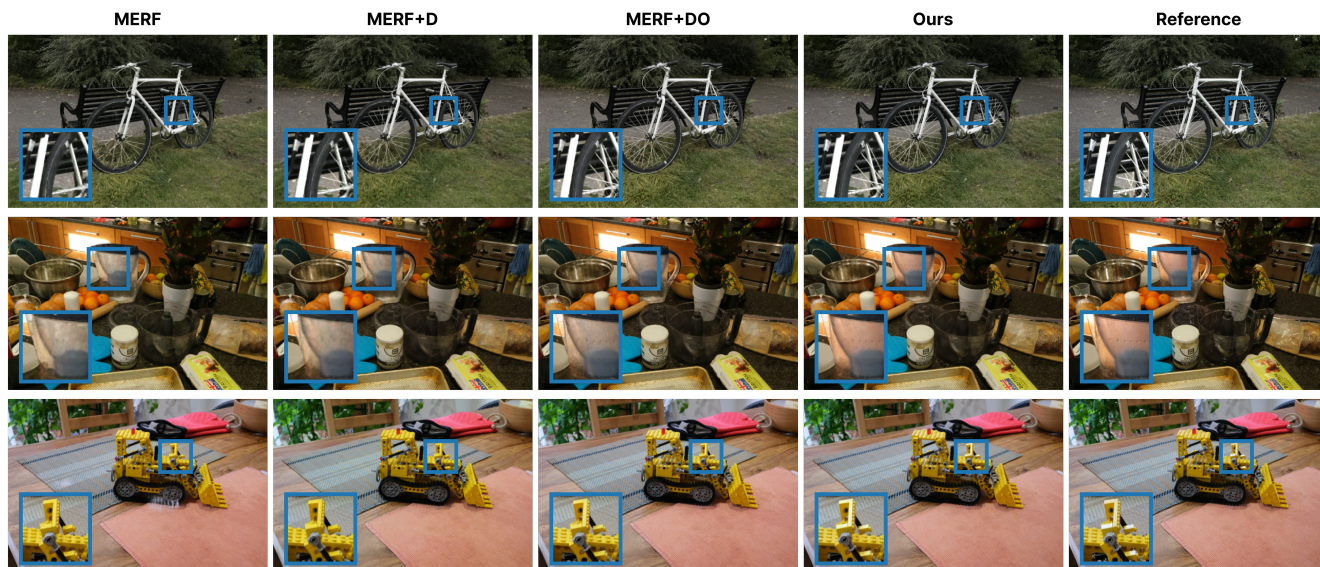


Figure 6. **Feature ablations.** We incrementally add distillation (MERF+D), optimization (MERF+DO), and model contributions (Ours) from Tab. 3 to MERF to reach our submodel architecture. Distillation and optimization contributions markedly increase geometric and texture detail while model contributions improve view-dependent modeling accuracy.

[14] Zhiwen Fan, Kevin Wang, Kairun Wen, Zehao Zhu, De-jia Xu, and Zhangyang Wang. LightGaussian: Unbounded 3d Gaussian compression with 15x reduction and 200+ fps.

arXiv, 2023.

[15] John Flynn, Michael Broxton, Paul Debevec, Matthew Duvall, Graham Fyffe, Ryan Overbeck, Noah Snavely, and

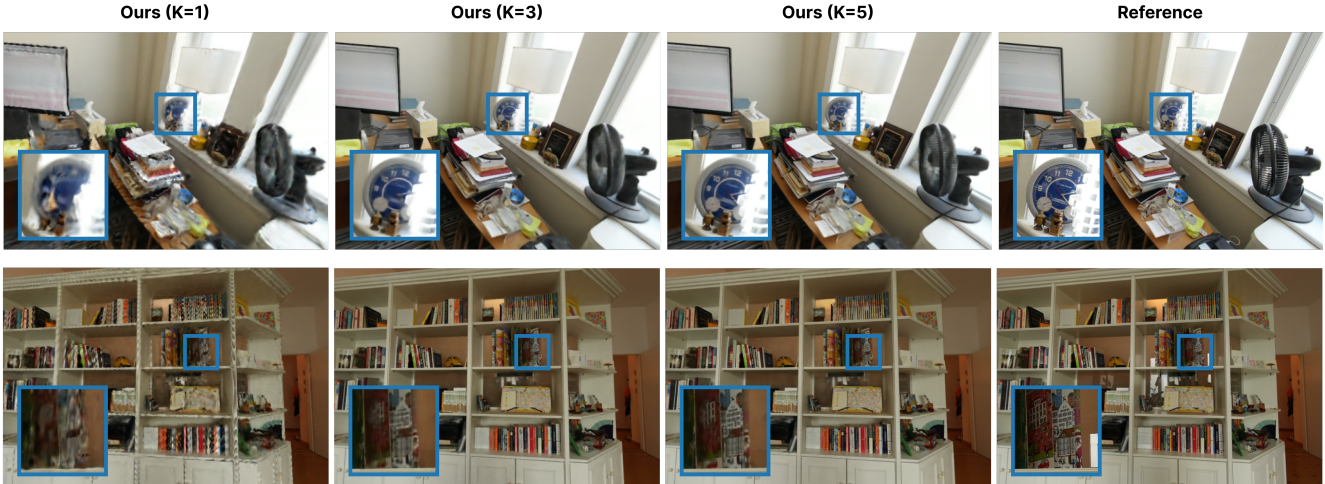


Figure 7. **Submodel resolution.** Increasing submodel spatial resolution naturally leads to increased visual fidelity, particularly with respect to high-frequency textures.

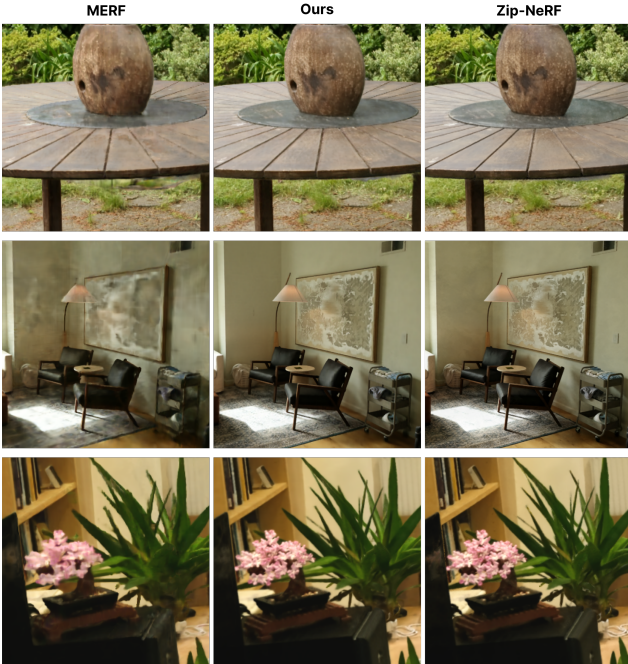


Figure 8. **Comparison to Zip-NeRF.** The rendering quality of our model approaches that of its Zip-NeRF teacher, while MERF exhibits various artifacts (top: a “bulging” table underside, middle: “smudged” appearance, bottom: lack of geometric detail). Our method is nearly indistinguishable from Zip-NeRF.

Richard Tucker. DeepView: View synthesis with learned gradient descent. *CVPR*, 2019.

- [16] Stephan J. Garbin, Marek Kowalski, Matthew Johnson, Jamie Shotton, and Julien Valentin. FastNeRF: High-fidelity neural rendering at 200fps. *ICCV*, 2021.
- [17] Jianping Gou, Baosheng Yu, Stephen J Maybank, and



Figure 9. **Submodel consistency.** We show renderings of the same camera from four different submodels. Despite having independent representations, our data augmentation and submodel consistency loss yield near-identical renderings.

Dacheng Tao. Knowledge distillation: A survey. *IJCV*, 2021.

- [18] Aarush Gupta, Junli Cao, Chaoyang Wang, Ju Hu, Sergey Tulyakov, Jian Ren, and László A Jeni. LightSpeed: Light and fast neural light fields on mobile devices. *arXiv*, 2023.
- [19] Kunal Gupta, Miloš Hašan, Zexiang Xu, Fujun Luan, Kalyan Sunkavalli, Xin Sun, Manmohan Chandraker, and Sai Bi. MCNeRF: Monte carlo rendering and denoising for real-time nerfs. *SIGGRAPH Asia*, 2023.
- [20] Peter Hedman, Julien Philip, True Price, Jan-Michael Frahm, George Drettakis, and Gabriel Brostow. Deep blending for free-viewpoint image-based rendering. *SIGGRAPH Asia*, 2018.
- [21] Peter Hedman, Pratul P. Srinivasan, Ben Mildenhall, Jonathan T. Barron, and Paul Debevec. Baking neural radiance fields for real-time view synthesis. *ICCV*, 2021.
- [22] Geoffrey Hinton, Oriol Vinyals, and Jeff Dean. Distilling the knowledge in a neural network. *arXiv:1503.02531*, 2015.

- [23] Wenbo Hu, Yuling Wang, Lin Ma, Bangbang Yang, Lin Gao, Xiao Liu, and Yuewen Ma. Tri-miprf: Tri-mip representation for efficient anti-aliasing neural radiance fields. In *Proceedings of the IEEE/CVF International Conference on Computer Vision*, pages 19774–19783, 2023.
- [24] Yifan Jiang, Peter Hedman, Ben Mildenhall, DeJia Xu, Jonathan T Barron, Zhangyang Wang, and Tianfan Xue. Alignerf: High-fidelity neural radiance fields via alignment-aware training. In *Proceedings of the IEEE/CVF Conference on Computer Vision and Pattern Recognition*, pages 46–55, 2023.
- [25] Bernhard Kerbl, Georgios Kopanas, Thomas Leimkühler, and George Drettakis. 3D Gaussian splatting for real-time radiance field rendering. *SIGGRAPH*, 2023.
- [26] Georgios Kopanas, Julien Philip, Thomas Leimkühler, and George Drettakis. Point-based neural rendering with per-view optimization. *Computer Graphics Forum*, 2021.
- [27] Andreas Kurz, Thomas Neff, Zhaoyang Lv, Michael Zollhöfer, and Markus Steinberger. AdaNeRF: Adaptive sampling for real-time rendering of neural radiance fields. *ECCV*, 2022.
- [28] Kevin Kwok. splat, 2023. <https://github.com/antimatter15/splat>.
- [29] Chen-Hsuan Lin, Wei-Chiu Ma, Antonio Torralba, and Simon Lucey. Barf: Bundle-adjusting neural radiance fields. In *Proceedings of the IEEE/CVF International Conference on Computer Vision*, pages 5741–5751, 2021.
- [30] Jeffrey Yunfan Liu, Yun Chen, Ze Yang, Jingkan Wang, Sivabalan Manivasagam, and Raquel Urtasun. Real-time neural rasterization for large scenes. *CVPR*, 2023.
- [31] Ricardo Martin-Brualla, Rohit Pandey, Shuoran Yang, Pavel Pidlypenskyi, Jonathan Taylor, Julien Valentin, Sameh Khamis, Philip Davidson, Anastasia Tkach, Peter Lincoln, et al. Lookingood: Enhancing performance capture with real-time neural re-rendering. *arXiv preprint arXiv:1811.05029*, 2018.
- [32] Ricardo Martin-Brualla, Noha Radwan, Mehdi S. M. Sajjadi, Jonathan T. Barron, Alexey Dosovitskiy, and Daniel Duckworth. NeRF in the wild: Neural radiance fields for unconstrained photo collections. *CVPR*, 2021.
- [33] Nelson Max. Optical models for direct volume rendering. *IEEE TVCG*, 1995.
- [34] Andreas Meuleman, Yu-Lun Liu, Chen Gao, Jia-Bin Huang, Changil Kim, Min H. Kim, and Johannes Kopf. Progressively optimized local radiance fields for robust view synthesis. *CVPR*, 2023.
- [35] Ben Mildenhall, Pratul P. Srinivasan, Rodrigo Ortiz-Cayon, Nima Khademi Kalantari, Ravi Ramamoorthi, Ren Ng, and Abhishek Kar. Local light field fusion: Practical view synthesis with prescriptive sampling guidelines. *ACM Transactions on Graphics*, 2019.
- [36] Ben Mildenhall, Pratul P. Srinivasan, Matthew Tancik, Jonathan T. Barron, Ravi Ramamoorthi, and Ren Ng. NeRF: Representing scenes as neural radiance fields for view synthesis. *ECCV*, 2020.
- [37] Thomas Müller, Alex Evans, Christoph Schied, and Alexander Keller. Instant neural graphics primitives with a multiresolution hash encoding. *SIGGRAPH*, 2022.
- [38] Thomas Neff, Pascal Stadlbauer, Mathias Parger, Andreas Kurz, Joerg H. Mueller, Chakravarty R. Alla Chaitanya, Anton Kaplanyan, and Markus Steinberger. DONeRF: Towards real-time rendering of compact neural radiance fields using depth oracle networks. *Computer Graphics Forum*, 2021.
- [39] Michael Niemeyer, Jonathan T. Barron, Ben Mildenhall, Mehdi S. M. Sajjadi, Andreas Geiger, and Noha Radwan. RegNeRF: Regularizing neural radiance fields for view synthesis from sparse inputs. *CVPR*, 2022.
- [40] Keunhong Park, Utkarsh Sinha, Jonathan T. Barron, Sofien Bouaziz, Dan B Goldman, Steven M. Seitz, and Ricardo Martin-Brualla. Nerfies: Deformable neural radiance fields. *ICCV*, 2021.
- [41] Keunhong Park, Philipp Henzler, Ben Mildenhall, Jonathan T. Barron, and Ricardo Martin-Brualla. Camp: Camera preconditioning for neural radiance fields. *SIGGRAPH Asia*, 2023.
- [42] Eric Penner and Li Zhang. Soft 3D reconstruction for view synthesis. *SIGGRAPH Asia*, 2017.
- [43] Hanspeter Pfister, Matthias Zwicker, Jeroen Van Baar, and Markus Gross. Surfels: Surface elements as rendering primitives. *SIGGRAPH*, 2000.
- [44] Julien Philip and Valentin Deschaintre. Floaters no more: Radiance field gradient scaling for improved near-camera training. *Eurographics Symposium on Rendering*, 2023.
- [45] Marie-Julie Rakotosaona, Fabian Manhardt, Diego Martin Arroyo, Michael Niemeyer, Abhijit Kundu, and Federico Tombari. NeRFMeshing: Distilling neural radiance fields into geometrically-accurate 3d meshes. *3DV*, 2023.
- [46] Daniel Rebain, Wei Jiang, Soroosh Yazdani, Ke Li, Kwang Moo Yi, and Andrea Tagliasacchi. DeRF: Decomposed radiance fields. *CVPR*, 2019.
- [47] Christian Reiser, Songyou Peng, Yiyi Liao, and Andreas Geiger. KiloNeRF: Speeding up neural radiance fields with thousands of tiny MLPs. *ICCV*, 2021.
- [48] Christian Reiser, Richard Szeliski, Dor Verbin, Pratul P. Srinivasan, Ben Mildenhall, Andreas Geiger, Jonathan T. Barron, and Peter Hedman. MERF: Memory-efficient radiance fields for real-time view synthesis in unbounded scenes. *SIGGRAPH*, 2023.
- [49] Konstantinos Rematas, Andrew Liu, Pratul P. Srinivasan, Jonathan T. Barron, Andrea Tagliasacchi, Thomas Funkhouser, and Vittorio Ferrari. Urban radiance fields. In *Proceedings of the IEEE/CVF Conference on Computer Vision and Pattern Recognition*, pages 12932–12942, 2022.
- [50] Barbara Roessle, Norman Müller, Lorenzo Porzi, Samuel Rota Bulò, Peter Kotschieder, and Matthias Nießner. GANeRF: Leveraging discriminators to optimize neural radiance fields. *SIGGRAPH Asia*, 2023.
- [51] Sara Rojas, Jesus Zarzar, Juan C Pérez, Artsiom Sanakoyeu, Ali Thabet, Albert Pumarola, and Bernard Ghanem. ReReND: Real-time rendering of NeRFs across devices. *CVPR*, 2023.
- [52] Darius Rückert, Linus Franke, and Marc Stamminger. ADOP: Approximate differentiable one-pixel point rendering. *SIGGRAPH*, 2022.
- [53] Johannes Lutz Schönberger and Jan-Michael Frahm. Structure-from-motion revisited. *CVPR*, 2016.

- [54] Liang Song, Guangming Wang, Jiuming Liu, Zhenyang Fu, Yanzi Miao, et al. Sc-nerf: Self-correcting neural radiance field with sparse views. *arXiv preprint arXiv:2309.05028*, 2023.
- [55] Pratul P. Srinivasan, Boyang Deng, Xiuming Zhang, Matthew Tancik, Ben Mildenhall, and Jonathan T. Barron. NeRV: Neural reflectance and visibility fields for relighting and view synthesis. *CVPR*, 2021.
- [56] Cheng Sun, Min Sun, and Hwann-Tzong Chen. Direct voxel grid optimization: Super-fast convergence for radiance fields reconstruction. *CVPR*, 2022.
- [57] Richard Szeliski and David Tonnesen. Surface modeling with oriented particle systems. *SIGGRAPH*, 1992.
- [58] Matthew Tancik, Vincent Casser, Xinchun Yan, Sabeek Pradhan, Ben Mildenhall, Pratul Srinivasan, Jonathan T. Barron, and Henrik Kretzschmar. Block-NeRF: Scalable large scene neural view synthesis. *CVPR*, 2022.
- [59] Ayush Tewari, Justus Thies, Ben Mildenhall, Pratul Srinivasan, Edgar Tretschk, W Yifan, Christoph Lassner, Vincent Sitzmann, Ricardo Martin-Brualla, Stephen Lombardi, et al. Advances in neural rendering. *Computer Graphics Forum*, 2022.
- [60] Haithem Turki, Deva Ramanan, and Mahadev Satyanarayanan. Mega-NeRF: Scalable construction of large-scale nerfs for virtual fly-throughs. *CVPR*, 2022.
- [61] Haithem Turki, Vasu Agrawal, Samuel Rota Bulò, Lorenzo Porzi, Peter Kotschieder, Deva Ramanan, Michael Zollhöfer, and Christian Richardt. HybridNeRF: Efficient neural rendering via adaptive volumetric surfaces. *arXiv*, 2023.
- [62] Ashish Vaswani, Noam Shazeer, Niki Parmar, Jakob Uszkoreit, Llion Jones, Aidan N Gomez, Łukasz Kaiser, and Illia Polosukhin. Attention is all you need. *NeurIPS*, 2017.
- [63] Ziyu Wan, Christian Richardt, Aljaž Božič, Chao Li, Vijay Rengarajan, Seonghyeon Nam, Xiaoyu Xiang, Tuotuo Li, Bo Zhu, Rakesh Ranjan, and Jing Liao. Learning neural duplex radiance fields for real-time view synthesis. *CVPR*, 2023.
- [64] Huan Wang, Jian Ren, Zeng Huang, Kyle Olszewski, Menglei Chai, Yun Fu, and Sergey Tulyakov. R2L: Distilling neural radiance field to neural light field for efficient novel view synthesis. *ECCV*, 2022.
- [65] Peng Wang, Lingjie Liu, Yuan Liu, Christian Theobalt, Taku Komura, and Wenping Wang. NeuS: Learning neural implicit surfaces by volume rendering for multi-view reconstruction. *NeurIPS*, 2021.
- [66] Zian Wang, Tianchang Shen, Merlin Nimier-David, Nicholas Sharp, Jun Gao, Alexander Keller, Sanja Fidler, Thomas Müller, and Zan Gojcic. Adaptive shells for efficient neural radiance field rendering. *SIGGRAPH Asia*, 2023.
- [67] Olivia Wiles, Georgia Gkioxari, Richard Szeliski, and Justin Johnson. Synsin: End-to-end view synthesis from a single image. *CVPR*, 2020.
- [68] Liwen Wu, Jae Yong Lee, Anand Bhattad, Yuxiong Wang, and David Forsyth. DIVEr: Real-time and accurate neural radiance fields with deterministic integration for volume rendering. *CVPR*, 2022.
- [69] Rundi Wu, Ben Mildenhall, Philipp Henzler, Keunhong Park, Ruiqi Gao, Daniel Watson, Pratul P. Srinivasan, Dor Verbin, Jonathan T. Barron, Ben Poole, and Aleksander Holynski. ReconFusion: 3d reconstruction with diffusion priors. *arXiv*, 2023.
- [70] Xiuchao Wu, Jiamin Xu, Zihan Zhu, Hujun Bao, Qixing Huang, James Tompkin, and Weiwei Xu. Scalable neural indoor scene rendering. *ACM TOG*, 2022.
- [71] Xiuchao Wu, Jiamin Xu, Xin Zhang, Hujun Bao, Qixing Huang, Yujun Shen, James Tompkin, and Weiwei Xu. ScaNeRF: Scalable bundle-adjusting neural radiance fields for large-scale scene rendering. *ACM Transactions on Graphics (TOG)*, 2023.
- [72] Linning Xu, Vasu Agrawal, William Laney, Tony Garcia, Aayush Bansal, Changil Kim, Samuel Rota Bulò, Lorenzo Porzi, Peter Kotschieder, Aljaž Božič, Dahua Lin, Michael Zollhöfer, and Christian Richardt. VR-NeRF: High-fidelity virtualized walkable spaces. *SIGGRAPH Asia*, 2023.
- [73] Han Yan, Celong Liu, Chao Ma, and Xing Mei. PlenVDB: Memory efficient vdb-based radiance fields for fast training and rendering. In *CVPR*, 2023.
- [74] Jiawei Yang, Marco Pavone, and Yue Wang. Freenerf: Improving few-shot neural rendering with free frequency regularization. In *Proceedings of the IEEE/CVF Conference on Computer Vision and Pattern Recognition*, pages 8254–8263, 2023.
- [75] Lior Yariv, Peter Hedman, Christian Reiser, Dor Verbin, Pratul P. Srinivasan, Richard Szeliski, Jonathan T. Barron, and Ben Mildenhall. BakedSDF: Meshing neural SDFs for real-time view synthesis. *SIGGRAPH*, 2023.
- [76] Alex Yu, Ruilong Li, Matthew Tancik, Hao Li, Ren Ng, and Angjoo Kanazawa. PlenOctrees for real-time rendering of neural radiance fields. *ICCV*, 2021.
- [77] Alex Yu, Sara Fridovich-Keil, Matthew Tancik, Qinhong Chen, Benjamin Recht, and Angjoo Kanazawa. Plenoxels: Radiance fields without neural networks. *CVPR*, 2022.
- [78] Kai Zhang, Gernot Riegler, Noah Snavely, and Vladlen Koltun. NeRF++: Analyzing and improving neural radiance fields. *arXiv:2010.07492*, 2020.
- [79] Qiang Zhang, Seung-Hwan Baek, Szymon Rusinkiewicz, and Felix Heide. Differentiable point-based radiance fields for efficient view synthesis. *SIGGRAPH Asia*, 2022.
- [80] Tinghui Zhou, Richard Tucker, John Flynn, Graham Fyffe, and Noah Snavely. Stereo magnification: Learning view synthesis using multiplane images. *SIGGRAPH*, 2018.
- [81] Matthias Zwicker, Hanspeter Pfister, Jeroen Van Baar, and Markus Gross. Surface splatting. *SIGGRAPH*, 2001.
- [82] Jakub Červený. gsplat — 3D gaussian splatting WebGL viewer, 2023. <https://gsplat.tech/>.